Available online at www.sciencedirect.com
SCIENCE DIRECT®
PERGAMON
International Journal of Heat and Mass Transfer 46 (2003) 3265–3278
International Journal of HEAT and MASS TRANSFER
www.elsevier.com/locate/ijhmt

A general formula for the evaluation of thermodynamic and aerodynamic losses in nucleating steam flow

M.J. Kermani *, A.G. Gerber

Department of Mechanical Engineering, University of New Brunswick, Fredericton, Canada E3B 5A3

Received 27 September 2002; received in revised form 18 January 2003

Abstract

Near saturation steam undergoing rapid expansion, with homogeneous nucleation of water droplets, is numerically studied in a series of converging/diverging nozzles with and without shocks. To understand loss mechanisms in such flows a numerical model is presented to calculate thermodynamic losses, which is further used to quantify associated total aerodynamic losses. For the converging/diverging nozzle configuration, the model shows that the overall thermodynamic loss is only mildly influenced by increasing shock strength, while the aerodynamic losses follow that of the single phase flow, and are of the same magnitude as the thermodynamic loss only in the case of very weak shocks. The thermodynamic losses can be attributed to two influences, the homogeneous nucleation event, and the post-shock thermal oscillations in the two-phase system. The calculations rely on a new two-phase CFD model, previously reported, for non-equilibrium phase change with droplet nucleation applicable to general 3D flow configurations.

Keywords: Thermodynamic losses; Aerodynamic losses; Nucleating steam; Eulerian–Lagrangian; Two phase flows

1. Introduction

In the design of industrial equipment utilizing fluid flow, obtaining a high efficiency of operation of the flow path often has a direct impact on the profitability of a plant. A loss in efficiency corresponds to a loss in the ability to do useful work, and for some devices, such as a steam turbine for example, this loss can accumulate over the run of a year into a significant impact on profitability. Assessing the mechanisms that lead to loss in available work is particularly difficult in highly compressible multiphase flows as found, for example, in the low-pressure end of a multistage steam turbine. In these transonic flows losses originate from interactions at boundaries (boundary layers), discontinuities in the flow properties (shocks), irreversible heat transfer associated with phase change, and losses generated with slip between different phases in the flow. To be able to quantify these losses and make appropriate design changes is a difficult task, particularly in highly three-dimensional (3D) flows. To assist in this objective a number of researchers have developed computational-fluid-dynamics models to be used in understanding these flows. A popular approach has been the methods based on inviscid time-marching schemes such as that presented in [1,2], however these have been limited to 2D cases and to very small droplet sizes. Recently another approach was developed by Gerber as reported in [3] based on the full Navier-Stokes equations and the use of interphase source terms to handle the interaction between phases. This approach was applied to 2D and 3D systems and is expandable to large droplet sizes where slip is present.

Experimental investigations have been undertaken to quantify the thermodynamic losses prevalent in transonic flows with phase change in steam systems [4,5]. The experimental work focused on flows in steam turbine blading and had the important aim of providing validation for the CFD models under development. Predictions of entropy generation due to non-equilibrium

* Corresponding author.
E-mail addresses: m.kermani@unb.ca (M.J. Kermani), agerber@unb.ca (A.G. Gerber).

0017-9310/03/$ - see front matter
doi:10.1016/S0017-9310(03)00096-6

Nomenclature

A	area (m^2)
c_p	liquid particle specific heat or vapor specific heat at constant pressure (J/kg K)
c_v	vapor specific heat at constant volume (J/kg K)
d	diameter (m)
H	vapor total enthalpy (J/kg)
h	static enthalpy (J/kg)
$\bar{h}$	average static enthalpy (J/kg)
J	nucleation rate (# droplets/m^3 s)
k	thermal conductivity (W/m K)
K	Boltzmann's constant ($=1.3807\times10^{-23}$ J/K)
Kn	Knudsen number ($=\hat{l}/d$)
l	local latent heat ($=h_g-h_p$) (J/kg)
L	equilibrium latent heat ($=h_{fg}$) at local pressure (J/kg)
$\hat{l}$	molecular mean free path (m)
m	mass (kg), mass of one molecule of water (kg), or counter for droplet numbers
M	Mach number or overall number of droplet groups
$\dot{m}$	mass flow rate (kg/s)
n	counter for droplet time steps
N	overall number of time steps
$\dot{n}$	droplet flow rate (# droplets/s)
Nu	Nusselt number ($=\alpha d/k$)
P	pressure (N/m^2)
Pr	Prandtl number ($=\mu c_p/k$)
q	conductive heat flux (W/m^2)
$\dot{Q}$	heat flow rate (W)
r	droplet radius (m)
r^*	droplet critical radius (droplet radius at nucleation) (m)
R	gas constant ($=461.4$ J/kg K)
S_h	source term for energy equation (W/m^3)
S_m	source term for mass equation (kg/m^3 s)
S_u	source term for momentum equation (N/m^3)
t	time (s)
T	temperature (K)
u	velocity (m/s)
$\overline{V}$	average velocity of droplet (m/s) (Fig. 2)
Vol	volume of a single control volume (m^3)
x	spatial dimension (m)

Greek symbols

α	convective heat transfer coefficient (W/m^2 K)
β	empirical adjustable parameter for droplet growth (Eq. (11) and Fig. 3)
γ	vapor specific heat ratio (≈1.32)
δm_p	mass growth of droplet (kg) (Fig. 2)
δQ	heat crossing the boundaries of Regions 1–3 (J) (Fig. 2)
$\delta\dot{q}$	heat flow rate of droplet group ($=\dot{n}\delta Q$) (W)
δt	time step (s) (Eq. (2) and Fig. 2)
ΔS	entropy rise (J/K)
ΔT	supercooling level ($=T_{sat}-T_g$) (K)
ϵ	turbulent dissipation (m^2/s^3)
η	correction parameter (Eq. (5))
κ	turbulent kinetic energy (m^2/s^2)
μ	dynamic viscosity (kg/m s)
ν	Nusselt correction (Eq. (9))
ρ	density (kg/m^3)
σ	liquid surface tension (N/m)
$\dot{\sigma}$	entropy generation rate (W/K) (Eq. (27))
τ	stress (N/m^2)
Ω	surface tension ratio ($=\sigma/\sigma_b$) (Fig. 3)

Subscripts

0	total state condition
1–3	Regions 1–3 (Fig. 2)
ae	aerodynamic losses
av	used for temperature averaging
b	tabulated value of surface tension or back pressure value
CD	computational domain
f	frozen Mach number (Fig. 14) or fluid property
g	gas (vapor)
ij	tensor notation
in	inlet condition
N	nucleation location (Figs. 8 and 9)
p	droplet
sat	saturated state
t	imaginary "throat" following separation (Figs. 8–10)
th	thermodynamic losses

Superscripts

E	equilibrium
NE	non-equilibrium

heat transfer with nucleation have not been performed earlier in the context of a two-phase Eulerian–Lagrangian model.

The present paper investigates transonic condensing turbulent flows in 2D converging–diverging nozzles, and presents a model for quantifying the aerodynamic,

thermodynamic and total losses present. The calculations utilize the model of Ref. [3], and it is anticipated that the procedures developed are general and applicable to the more complex two-phase flow behavior found in devices such as steam turbines.

2. Mathematical modeling

The mathematical model developed for condensing steam relies on an Eulerian–Lagrangian representation of the two phase system. The two phases (vapor and liquid droplets) are treated as two independent flows, with the interaction between the phases applied through the source terms included in the continuity, momentum and energy equations of the vapor phase.

2.1. Eulerian (continuum) phase

The governing equations for the gas phase, referred to as the Eulerian phase, are:

$$\begin{aligned}
&\frac{\partial \rho}{\partial t}+\frac{\partial}{\partial x_j}(\rho u_j)=S_m,\\
&\frac{\partial \rho u_i}{\partial t}+\frac{\partial}{\partial x_j}(\rho u_j u_i)=-\frac{\partial P}{\partial x_i}+\frac{\partial \tau_{ij}}{\partial x_j}+S_{u_i},\\
&\frac{\partial \rho H}{\partial t}-\frac{\partial P}{\partial t}+\frac{\partial}{\partial x_j}(\rho u_j H)=-\frac{\partial q_j}{\partial x_j}+\frac{\partial}{\partial x_j}(u_i\tau_{ij})+S_h,
\end{aligned} \tag{1}$$

where ρ, u_i, P, H, q and τ denote gas phase conditions of density, i-wise velocity component, pressure, total enthalpy, conductive heat flux and shear stress respectively. The source terms S_m, S_{u_i}, and S_h contain the terms describing the mass, momentum and energy exchange between the phases, which are determined from:

$$\begin{aligned}
S_m&=\frac{1}{\mathrm{Vol}}\sum_m^M\sum_n^N\left[(\dot{m}_\mathrm{p})_{mn}^{t+\delta t}-(\dot{m}_\mathrm{p})_{mn}^{t}\right],\\
S_{u_i}&=\frac{1}{\mathrm{Vol}}\sum_m^M\sum_n^N\left[(\dot{m}_\mathrm{p}u_{i_\mathrm{p}})_{mn}^{t+\delta t}-(\dot{m}_\mathrm{p}u_{i_\mathrm{p}})_{mn}^{t}\right],\\
S_h&=\frac{1}{\mathrm{Vol}}\sum_m^M\sum_n^N\left[(\dot{m}_\mathrm{p}h_\mathrm{p})_{mn}^{t+\delta t}-(\dot{m}_\mathrm{p}h_\mathrm{p})_{mn}^{t}\right],
\end{aligned} \tag{2}$$

where the summations are over all, M, liquid droplet groups, each taking N time-steps to sweep the extent of a control volume. It is noted that the droplet integration time-step is independent of the gas phase time-step for the present steady state computations. In Eq. (2) the droplet enthalpy, h_p, is comprised of the bulk internal energy, the surface energy associated with a spherical droplet, and kinetic energy (complete details are available in [3]).

Turbulence is modeled via the standard κ–ϵ model [6]. The source terms in the κ–ϵ equations do not consider the influence of the liquid droplets on turbulence conditions. However, this effect is indirectly modeled via the velocity field introduced to the κ–ϵ equations in each iteration. This is assumed adequate for droplets of submicron in size.

2.2. Equation-of-state

The study of non-equilibrium thermodynamics (in the context of high-speed compressible flows) involves conditions of supercooled states, and an equation of state reliable for extrapolation into supercooled conditions must be utilized. In the present work the equation-of-state reported in [7] is used, which was tested for extrapolation into supercooled states [8]. This equation-of-state, utilizing a virial formulation, is reliable for both high and low pressure conditions ranging from 0.01 to 100 bar, and over a temperature range of 273.15–1000 K. While the present study will be limited to cases at low pressure (below 1 bar), the model is intended for application at high pressures as well and therefore a more extensive equation of state was implemented. The virial equation of state along with relations for vapor pressure, liquid density and specific heat data (described more fully in a previous study [9]) provides the basis for calculating all properties required in the simulations, for both equilibrium and supercooled states.

2.3. Lagrangian (dispersed) phase

The liquid phase is introduced into the flow on the basis of classical nucleation theory as described in [10], and once present, the trajectory of the droplets are determined on the basis of a Lagrangian motion model. In the present study all droplets are assumed to be small (<1 μm) having formed by homogenous nucleation. This allows a no slip condition to be imposed between vapor and droplet. That is, the droplet motion is determined solely by the gas (vapor) phase. The size of the droplet introduced into the flow is the critical radius calculated as [10]:

$$r^*=\frac{2\sigma T_\mathrm{sat}(P)}{\rho_\mathrm{f} L\Delta T}, \tag{3}$$

where σ is the surface tension, $T_\mathrm{sat}(P)$, saturation temperature at the local pressure, ρ_f, density of the liquid droplet, L, equilibrium latent heat, and ΔT, the supercooling level ($=T_\mathrm{sat}(P)-T_\mathrm{g}$; in which T_g is the gas temperature). The number of droplets associated with a droplet group integrated through the flow domain is calculated from the nucleation rate as:

$$J=\frac{1}{1+\eta}\left(\frac{2\sigma}{\pi m^3}\right)^{1/2}\frac{\rho_\mathrm{g}^2}{\rho_\mathrm{f}}\exp\left(-\frac{4\pi r^{*2}\sigma}{3KT_\mathrm{g}}\right), \tag{4}$$

where η is defined by:

$$\eta = 2\frac{\gamma-1}{\gamma+1}\frac{L}{RT_g}\left(\frac{L}{RT_g}-\frac{1}{2}\right) \tag{5}$$

and ρ_g is the gas (vapor) phase density, K, the Boltzmann's constant, m, the mass of one water molecule, R, the gas constant, and γ, the specific heat ratio ($\approx$1.32).

The droplet once released into the flow grows through heat, mass and momentum transfer with its surrounding vapor. To calculate the source term contributions to the gas phase equations (S_m, S_{u_i} and S_h) an energy equation for the droplet phase must be solved. This solution, on a single droplet basis, provides information on the growth of a droplet in either a supercooled or superheated environment. The energy equation is based on modeling latent heat requirements with phase change, convective heat transfer into or away from the liquid droplet, and the temperature change of the liquid droplet. This is described by the equation:

$$l\frac{dm_p}{dt} = \alpha_p A_p(T_p - T_g) + m_p c_p \frac{dT_p}{dt}, \tag{6}$$

where m_p is the mass of one liquid droplet ($=4/3\rho_f\pi r_p^3$, in which r_p is the radius of the liquid droplet), c_p, the specific heat of the liquid droplet, α_p, the convective heat transfer coefficient between a liquid droplet and its surroundings, A_p, the area of one liquid droplet ($=4\pi r_p^2$), and l is the local latent heat ($=h_g - h_p$).

For the present calculations, where all droplets remain very small (<1 μm), the contribution of the internal energy term in Eq. (6) can be ignored. Therefore, Eq. (6) reduces to:

$$(h_g - h_p)\frac{dm_p}{dt} = \alpha_p(4\pi r_p^2)(T_p - T_g) \tag{7}$$

or

$$(h_g - h_p)\frac{dr_p}{dt} = \alpha_p(T_p - T_g) \tag{8}$$

with the unknowns r_p and T_p. The heat transfer coefficient α_p is determined from the Nusselt number [11]:

$$Nu \equiv \frac{\alpha_p d_p}{k_g} = \frac{2}{1 + 3.78(1-v)Kn/Pr_g}, \tag{9}$$

where k_g is the thermal conductivity of gas (vapor), d_p, the diameter of a liquid droplet ($=2r_p$), Pr_g, the gas Prandtl number, and Kn, the Knudsen number defined by $Kn \equiv \hat{l}/d_p$, in which $\hat{l}$ is the mean free path of the gas molecules defined by:

$$\hat{l} = 1.5\mu_g\sqrt{RT_g}/P, \tag{10}$$

where μ_g is the dynamic viscosity of the gas. In Eq. (9), $(1-v)$ is a correction factor suggested in [12]:

$$v = \frac{RT_{sat}(P)}{L}\left[\beta - \frac{1}{2} - \frac{1}{2}\left(\frac{\gamma+1}{2(\gamma-1)}\right)\left(\frac{RT_{sat}(P)}{L}\right)\right], \tag{11}$$

where β is an empirical adjustable parameter. Solving Eq. (8) requires additional information to relate r_p and T_p. This would normally be done through a mass conservation equation. However, a simple algebraic equation, useful for steam is used to obtain the liquid droplet temperature [11]:

$$T_p = T_{sat}(P) - [T_{sat}(P) - T_g]\frac{r^*}{r_p}. \tag{12}$$

The preceding describes the governing equations applied to the nucleation and subsequent growth of the liquid droplet phase. The sequencing of these equations in conjunction with the gas phase equations follows the strategy:

1. The supercooling levels in the flow field ($\Delta T = T_{sat}(P) - T_g$) are calculated from the latest gas phase solution.
2. Based on supercooling levels the nucleation rate is calculated from Eq. (4) at every location in the flow domain.
3. At locations in the flow with significant nucleation ($J > 10^{15}$) a droplet group is introduced into the flow representative of numerous liquid droplets.
4. Integration of the droplet using the growth equations (Eqs. (8) and (12)) and the latest velocity field allows for the gas phase source terms to be computed.
5. The gas phase equations are then solved (Eq. (1)) using the calculated source term contributions from the droplet phase (repeat of step 1).
6. The entire procedure is repeated until steady-state behavior is reached.

Considerable detail is embodied in the above solution steps and the reader can refer to [3] if interested. In the present case the droplet integration also allows for the irreversible entropy rise, due to temperature differences between the phases, to be calculated. In a subsequent section a model to calculate this irreversibility will be presented and is the main contribution of this paper.

2.4. Boundary conditions

All calculations in the current study were performed on a series of nozzle geometries ((A), (B), (C) and (D)) as depicted in Fig. 1. The geometry of the expansion portion of these nozzles were taken to be the same as those used in the experiments of Moore et al. [13]. The boundary conditions specified in the calculations and the assumptions made were as follows:

- At the nozzle inflow, subsonic flow was specified using total pressure ($P_{0_{in}}$), total temperature ($T_{0_{in}}$) and flow angle normal to the inlet plane. In addition a

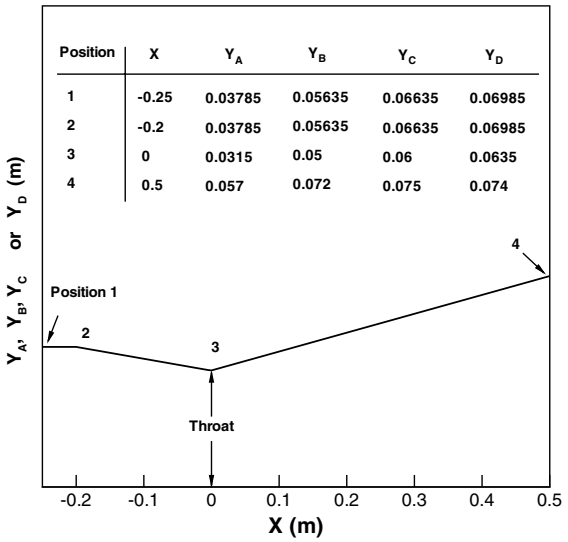

Fig. 1. Geometry of four different nozzles (A), (B), (C) or (D) used in the current studies.

turbulent intensity of 5%, and an eddy length scale of 7.5% of the nozzle inlet diameter were used.

- At the wall a no-slip adiabatic wall condition was used and it was assumed that the liquid droplets, upon impact with the wall, were reflected back into the flow with a coefficient of restitution equal to 0.1.
- Assuming that the flow is symmetrical about the nozzle centerline, symmetry conditions were enforced for all flow variables along this plane.
- At the exit plane, either supersonic or subsonic outflow conditions were applied. For supersonic outflow, all of the flow parameters were extrapolated from the interior of the domain to the exit plane. For subsonic outflow, pressure at the exit plane (back pressure (P_b)) was specified and the rest of the flow parameters were extrapolated from the interior of the domain.

2.5. Thermodynamic losses evaluation

The prevailing feature in a non-equilibrium flow is that the temperature of the phases differ. This difference in temperature is the source of irreversible heat transfer between phases. Subsequently, the entropy operation rate throughout the flow field becomes relatively substantial and is usually referred to as thermodynamic losses.

In the current study, the entropy rise associated with thermodynamic loss is calculated from the Lagrangian tracking model. In this approach particles are tracked throughout the computational domain and any associated entropy rise during the journey of particles are accumulated so that total entropy rises are evaluated.

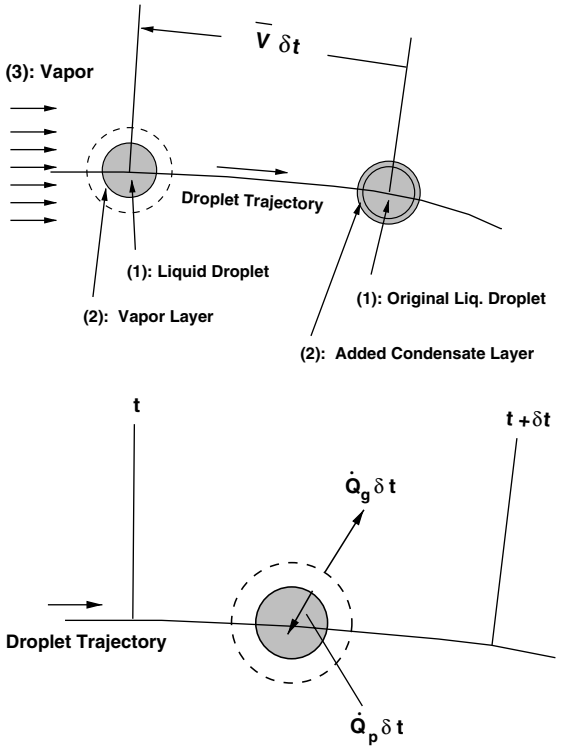

Fig. 2. (Top) Schematic of a liquid droplet, growing by condensation along its trajectory within the time step δt. (Bottom) The representation of latent heat release toward liquid droplet and/or vapor in a condensation process.

Fig. 2(top) shows a traveling liquid droplet in a continuum media of vapor, undergoing a continuous condensation process. In this figure, a liquid droplet travels the distance $\overline{V}\delta t$ along the vapor streamline. It is noted that $\overline{V}$ is the droplet average velocity within the time step δt (taken to be equal to that of the vapor in the present computation for small droplets, in which slip velocity is ignored). The enthalpy of the vapor phase, h_g, is assumed to be constant over the time step δt. However, an average enthalpy for the droplet, $\bar{h}_p$, is obtained over the time step δt.

To obtain a formula for the losses associated to irreversible heat transfer between the phases the system of liquid droplet and vapor is divided into three regions, as shown in Fig. 2(top). Regions 1 and 3 are respectively pure liquid and vapor, and remain the same phase throughout the condensation process (i.e. within the time step δt). However, the fluid layer of Region 2, is at first vapor and at the end of the time step is totally liquid (see Fig. 2(top)). As liquid is created it is added to Region 1, so at the end of the time step the vapor volume of Region 2 is zero. The state of the fluid in Region 2 is always on average of that in Regions 1 and 3.

To condense the vapor layer in Region 2, the latent heat associated with this layer, i.e. $\delta m_p(h_g - \bar{h}_p)$, should be released toward the liquid (Region 1) and/or vapor (Region 3), i.e.

$$\delta m_p(h_g - \bar{h}_p) = \dot{Q}_g \delta t + \dot{Q}_p \delta t \tag{13}$$

as shown in Fig. 2(bottom). In Eq. (13), $\dot{Q}_p$ and $\dot{Q}_g$ are the heat flow rates toward liquid droplet and vapor, respectively, and δm_p is the mass of fluid layer in Region 2. It is noted that Eqs. (6) and (13) are equivalent representation for the latent heat removal from the condensing layer, flowing toward liquid droplet and/or vapor, if Eq. (6) were integrated in time.

The entropy generation for a system consisting of Regions 1–3 is denoted by ΔS_{th}:

$$\Delta S_{th} = \Delta S_1 + \Delta S_2 + \Delta S_3, \tag{14}$$

where ΔS_1, ΔS_2, and ΔS_3 are the entropy generation within δt in Regions 1–3, respectively:

$$\Delta S_1 \equiv (S_{t+\delta t} - S_t)_1, \tag{15}$$

$$\Delta S_2 \equiv (S_{t+\delta t} - S_t)_2, \tag{16}$$

$$\Delta S_3 \equiv (S_{t+\delta t} - S_t)_3. \tag{17}$$

It is noted that the whole system containing Regions 1–3 are in a thermally non-equilibrium condition, however, we assume each individual phase is in equilibrium, undergoing an internally reversible process. Under this assumption the thermodynamic relation

$$\Delta S = \left(\frac{\delta Q}{T}\right)_{\text{internally reversible}} \tag{18}$$

could be used for each of the Regions 1–3:

$$\Delta S_1 = \frac{\dot{Q}_p \delta t}{\overline{T}_p}, \tag{19}$$

$$\Delta S_2 = -\frac{\delta m_p (h_g - \bar{h}_p)}{T_{av}}, \tag{20}$$

$$\Delta S_3 = \frac{\dot{Q}_g \delta t}{T_g}, \tag{21}$$

where T_{av} is the average temperature of the fluid layer in Region 2, which is bounded by the liquid temperature $\overline{T}_p$ and the vapor temperature T_g. In general the temperature difference between liquid and vapor is of the order of 10^1 in the rapid condensation zone, and 10^0 in the quasi-equilibrium conditions following this. To simplify the analysis either T_g or $\overline{T}_p$ can be used for T_{av} with a small loss in accuracy. This assumption must be reconsidered for larger droplet sizes (over 1 μm in size), since the temperature deviations between vapor and liquid can become even larger in a supercooled environment. In this paper T_{av} is set to T_p so that combining Eqs. (13), (14) and (19)–(21) we obtain:

$$\Delta S_{th} = \left[\delta m_p (h_g - \bar{h}_p) - \dot{Q}_p \delta t\right]\left(\frac{1}{T_g} - \frac{1}{\overline{T}_p}\right). \tag{22}$$

Eq. (22) gives the entropy rise associated with a single droplet traveling the time interval δt.

Along a streamline over which a droplet group is tracked there is a known rate of droplets transported ($\dot{n}$), so that where m_p appears we can apply $\dot{n} m_p = \dot{m}_p$ (note that a droplet group represents a large number of individual droplets associated with nucleation—see Step 3 in Section 2.3). Multiplying $\dot{n}$ into Eq. (22), the entropy generation rate for a droplet group along a streamline become:

$$\dot{n}\Delta S_{th} = \left[\delta \dot{m}_p (h_g - \bar{h}_p) - \dot{n}\delta Q_p\right]\left(\frac{1}{T_g} - \frac{1}{\overline{T}_p}\right), \tag{23}$$

where $\delta Q_p \equiv \dot{Q}_p \delta t$.

Tracking all of the liquid droplets and summing the associated thermodynamic losses over all time steps:

$$\left(\frac{DS}{Dt}\right)_{th} = \sum_m^M \sum_n^{N_{CD}} \left[\delta \dot{m}_p (h_g - \bar{h}_p) - \delta \dot{q}_p\right]_{mn} \times \left(\frac{1}{T_g} - \frac{1}{\overline{T}_p}\right)_{mn}, \tag{24}$$

where $\delta \dot{q}_p = \dot{n}\delta Q_p$, N_{CD} is the number of time steps from the time a droplet group begins (at nucleation) until it leaves the computational domain and M is the total number of droplet groups.

Eq. (24) gives the entropy generation rate due to irreversible heat transfer between the phases (i.e. thermodynamic losses as noted earlier). Eq. (24) was derived for a condensation process, in which $\delta \dot{m}_p$ is positive and the temperature of liquid droplet is more than that of the vapor, i.e. $(1/T_g - 1/\overline{T}_p) > 0$. Therefore, for a condensing process it is guaranteed that $(DS/Dt)_{th} > 0$. For an evaporation case, $\delta \dot{m}_p$ is negative and $(1/T_g - 1/\overline{T}_p)$ is also negative. This again guarantees $(DS/Dt)_{th} > 0$.

It is important to note that Eq. (24) is a general equation, in the derivation of which, a portion of latent heat is considered flowing toward the liquid droplet. Eq. (24) can be simplified to a form similar to that developed in [14] and applied in a mixture based single-phase approach, where the latent heat of the fluid layer of Region 2 was exclusively considered to move toward the vapor phase (see Fig. 2(bottom)). Dropping the term $\dot{q}_p$ in Eq. (24) results in:

$$\left(\frac{DS}{Dt}\right)_{th} = \sum_m^M \sum_n^{N_{CD}} \left[\delta \dot{m}_p (h_g - \bar{h}_p)\right]_{mn} \left(\frac{1}{T_g} - \frac{1}{\overline{T}_p}\right)_{mn}. \tag{25}$$

However, this simplification overestimates the thermodynamic losses, and furthermore, could lead to non-physical evaluation of aerodynamic losses determined from:

$$\left(\frac{DS}{Dt}\right)_{ae} = \dot{\sigma} - \left(\frac{DS}{Dt}\right)_{th}, \tag{26}$$

since a negative value for aerodynamic losses could be obtained in cases with small viscous losses. In Eq. (26), $\dot{\sigma}$ is the total entropy generation rate for an adiabatic steady flow, throughout the overall computational domain, determined by

$$\dot{\sigma} = \sum \dot{m}_e s_e - \sum \dot{m}_i s_i, \tag{27}$$

where s_e and s_i are mixture (liquid and vapor) properties at the exit and inlet of the domain.

It is noted that as an advantage of the two-phase Eulerian–Lagrangian approach, as adopted in the present computation, direct computation of the term $\delta\dot{q}_p$ in Eq. (24) is possible via the source term of the energy equation, S_h (see Eq. (2)) by simply setting $\delta\dot{q}_p = -(\delta S_h)(\mathrm{Vol})$. Integrating over all the droplet groups and all the time steps sweeping the extent of a control volume, one can obtain: $S_h = -(\sum_m^M \sum_n^N \delta\dot{q}_p)/(\mathrm{Vol})$.

It should be emphasized that in non-equilibrium modeling, in order to precisely estimate aerodynamic losses using an equation similar to Eq. (26), an accurate evaluation of thermodynamic loss is always necessary. It will be shown later in this paper that the estimation of thermodynamic loss can deteriorate about 10% (for the geometry considered in this paper) by dropping of $\dot{q}_p$ (or $\delta\dot{q}_p$) in the evaluation of $(DS/Dt)_{th}$ (see Figs. 13 and 14). An assessment of Eq. (24) for use in Eq. (26) is performed in Section 3.2.

2.6. Solution algorithm

The non-equilibrium condensation model, described here and in [3], has been implemented by the authors within the commercial CFD code CFX-TASCflow, which provides the overall framework for the solution of the hydrodynamic equations. This software is spatially second-order accurate, and uses a finite-volume/finite-element discretization approach. The solution of the Eulerian equation set utilizes a coupled solution of the momentum and mass equations along with multigrid, resulting in a linear scaling in solution time with problem size (see Ref. [15]). The droplet integration scheme (the Lagrangian part) is based on a first-order forward Euler method.

3. Numerical validation

3.1. Comparison vs. experimental values in literature

Quantitative validation of the numerical model is accomplished using four different geometries (labeled as nozzles (A), (B), (C), and (D) in Fig. 1) based on the experiments of [13]. The nucleation model used in this paper has been applied widely for steam and exhibits a strong sensitivity to the value of surface tension, σ (see Eq. (4)), and as suggested in the work of [13], some numerical testing is required to obtain the best value. Furthermore, to improve predictions at lower pressures $P < 0.4$ bar, the model of [1] was used, which introduces a further adjustable parameter β (see Eq. (11)) applied to the droplet energy equation.

To establish acceptable values for Ω and β (Ω being the surface tension ratio equal to σ/σ_b, where σ_b is the tabulated bulk surface tension), a systematic approach has been taken to minimize errors. The approach involves selecting a matrix of values for Ω and β to cover a reasonable range for these parameters. A matrix of calculations was then performed for nozzles (A) and (C) using combinations of Ω and β. The computed centerline pressure for each of the calculations was compared with that of the experiment, obtained in [13], and an RMS error between the computed results and experimental values are calculated. For the matrix of calculations the RMS errors are shown in Fig. 3 for both of the nozzles (A) and (C). As shown in this figure the region of lowest error for nozzles (A) and (C) overlap each other in the vicinity of $\Omega = 0.9$ and $\beta = 5$. The same values for Ω and β are used for the two other nozzles, (B) and (D), and the pressure distribution along the centerline are compared with experimental values, as shown in Fig. 4. As it is apparent in this figure, the final result is in excellent agreement with experiment for all four nozzles. Fig. 5

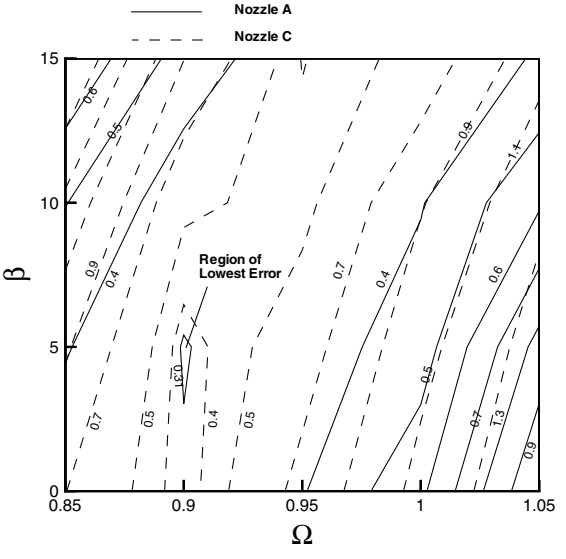

Fig. 3. RMS of relative error of centerline pressure vs. experimental values of Moore et al. (1973) for nozzles (A) and (C). The lowest error region for both of the nozzles overlap each other (on $\Omega = 0.9$ and $\beta = 5$).

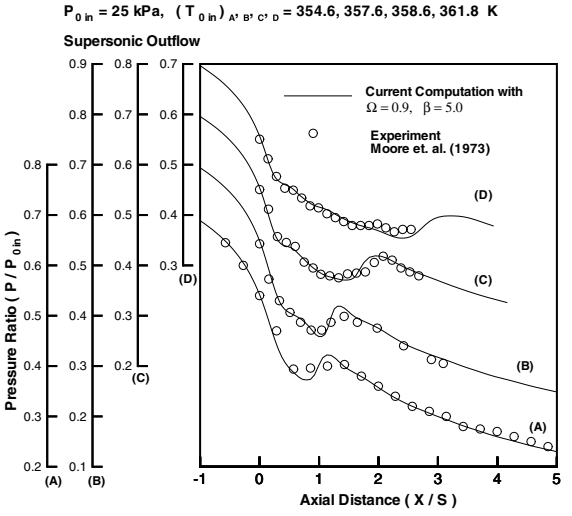

Fig. 4. Comparisons of pressure distribution along the nozzle centerline, for nozzles (A) to (D).

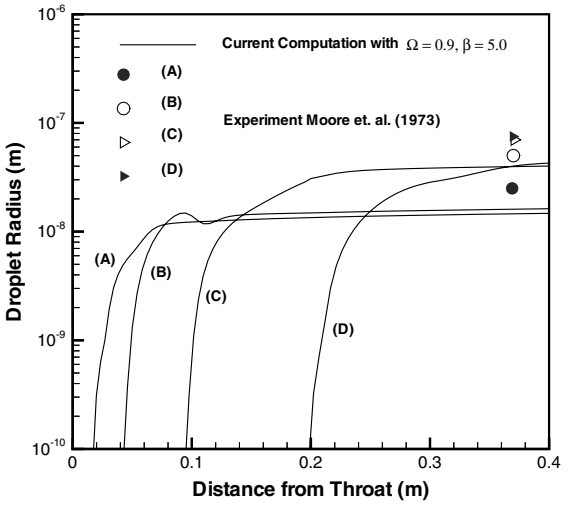

Fig. 5. Comparison of droplet radius at specified location for nozzles (A) to (D) with supersonic outflow.

shows the distribution of droplet radius compared to that of [13] given at a single location. The agreement of computed droplet radius with experiment are reasonable considering that there is still considerable uncertainty in the measurement of droplet sizes at this scale. As a further verification, the value of β obtained using this procedure is consistent with the recommendation of [1].

3.2. Thermodynamic losses verification

Verification of the formula for thermodynamic losses, derived in Section 2.5 and described by Eq. (24), is performed on the basis of a self-consistency test between non-equilibrium and equilibrium solution loss predictions. To do this verification aerodynamic losses are evaluated using two different physical models for the energy exchange between the phases, namely: (i) thermal non-equilibrium with interphase exchange as described in the mathematical modeling section, and (ii) thermal equilibrium where no Lagrangian solution is required and the moisture content (wetness) is obtained from the equilibrium phase diagram (and all properties are updated according to standard mixture rules). It is expected that the aerodynamic losses obtained using the physical models (i) and (ii) to be comparable if the mass flows are the same.

In non-equilibrium flows the aerodynamic losses can be evaluated using Eq. (26), while for the equilibrium solution there is no thermodynamic losses because the phases are in thermal equilibrium. Therefore, the aerodynamic losses of equilibrium flows are equal to the total losses (for adiabatic and steady flows) so that,

$$\left(\frac{\mathrm{D}S}{\mathrm{D}t}\right)_{\mathrm{ae}}^{\mathrm{E}} = \dot{\sigma}^{\mathrm{E}}. \tag{28}$$

To properly compare the equilibrium and non-equilibrium loss predictions it should be ensured that the mass flow for the cases are same. Similar inflow boundary conditions do not guarantee the same mass flow through the nozzle since equilibrium condensation may begin just before the throat. To obtain the same mass flow for equilibrium and non-equilibrium cases, a nozzle is chosen similar to that of [16], with boundary conditions $P_{0_{\mathrm{in}}} = 100$ kPa, and $T_{0_{\mathrm{in}}} = 413.15$ K, and supersonic outflow condition. Fig. 6 shows the nozzle

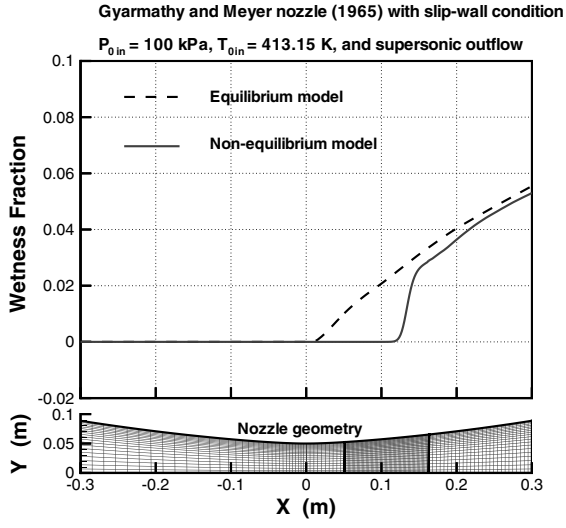

Fig. 6. Gyarmathy and Meyer nozzle (1965), and wetness fraction profile along the nozzle centerline, obtained by present computation using equilibrium and non-equilibrium models.

Table 1
Comparison of aerodynamic losses using equilibrium and non-equilibrium models

Case	$\dot{\sigma}^{NE}$ (Eq. (27))	$(DS/Dt)_{th}$ (Eq. (24))	$(DS/Dt)_{ae}^{NE}$ (Eq. (26))	$(DS/Dt)_{ae}^{E}$ (Eq. (28))	Δ_{ae}[a]
a (slip wall)	0.7161	0.6900	0.0261	0.0247	0.0014
b (no slip wall)	1.4420	0.6768	0.7652	0.7000	0.0652

[a] $\Delta_{ae} = (DS/Dt)_{ae}^{NE} - (DS/Dt)_{ae}^{E}$.

geometry and profile of the wetness fraction along the nozzle centerline, computed by equilibrium and non-equilibrium models. As shown in this figure, condensation for both models occur downstream of the throat and that the wetness of the non-equilibrium model nearly recovers the equilibrium value, the difference being due to the higher exit entropy level with a non-equilibrium flow (for the same back pressure).

To test for physically realistic trends, the equilibrium and non-equilibrium loss predictions are obtained for two different wall boundary conditions: (a) with slip wall conditions and (b) a case with no-slip wall conditions. In case (a) the near wall viscous losses are eliminated and therefore the predicted aerodynamic losses should drop significantly. The predicted aerodynamic losses for the cases (a) and (b) (in terms of W/K) are summarized in Table 1.

The non-equilibrium aerodynamic loss predictions as expected approach the equilibrium values but remain slightly larger. The difference is attributed to the condensation shock, as shown in Fig. 7, which adds an additional aerodynamic loss component similar to that of a mild shock. From the theory for oblique shocks (see Ref. [17] for example) an estimate of this loss can be made and is of the same order as the values for the predicted Δ_{ae}. A direct comparison cannot be made because the Mach number profile across the nozzle (in transverse direction) is not uniform as required by classical theory for oblique shocks.

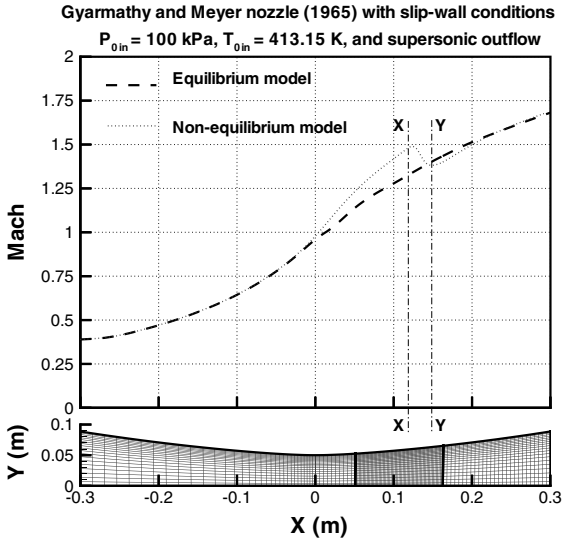

Fig. 7. Gyarmathy and Meyer nozzle (1965), and Mach number profile along the nozzle centerline, obtained by present computation using equilibrium and non-equilibrium models.

4. Results and discussions

4.1. Physical description of non-equilibrium steam flow with and without shocks

To qualitatively describe the physics of non-equilibrium condensing steam flow, with or without shocks, a sample of the calculated results for nozzle (A) are shown in Figs. 8 and 9. The boundary conditions for these results were $P_{0_{in}} = 25$ kPa and $T_{0_{in}} = 354.6$ K at the inflow, and either a supersonic outflow condition, or a specified back pressure of $P_b = 16$ kPa.

The computational grid used for the calculations was based on a grid independence test, in which three different grid densities were examined: 60×10, 100×20, and 180×40. It was observed that the grid density 100×20 can adequately capture the details of the flow, and was used for all of the results presented.

In Fig. 8(a) the distribution of supercooling, $\Delta T = T_{sat}(P) - T_g$, along the nozzle centerline is shown. With significant supercooling spontaneous nucleation of liquid droplets occurs at the nozzle location $x = x_N$. At this location a significant amount of liquid droplets are generated, approximately 10^{22} droplets per second per unit volume (see Fig. 8(c)). The size at which the droplets appear in the flow are generally of the order 10^{-10} m and grow very rapidly by condensation of vapor on the droplet surface. The distribution of wetness fraction and droplet radius along the nozzle centerline is shown in Fig. 8(b) and (d). At the nozzle location x_N a sharp rise in wetness fraction is observed, reflecting the rapid growth of the droplets immediately following the peak nucleation. Referring again to Fig. 8(a), it is shown that after peak nucleation, the supercooling level rapidly drops to near equilibrium conditions ($\Delta T \approx 1$–2 K). This near equilibrium condition prevails the remaining length of the nozzle for the supersonic outflow case. It should be noted that the small positive value of ΔT is a physical requirement to support latent heat release toward the

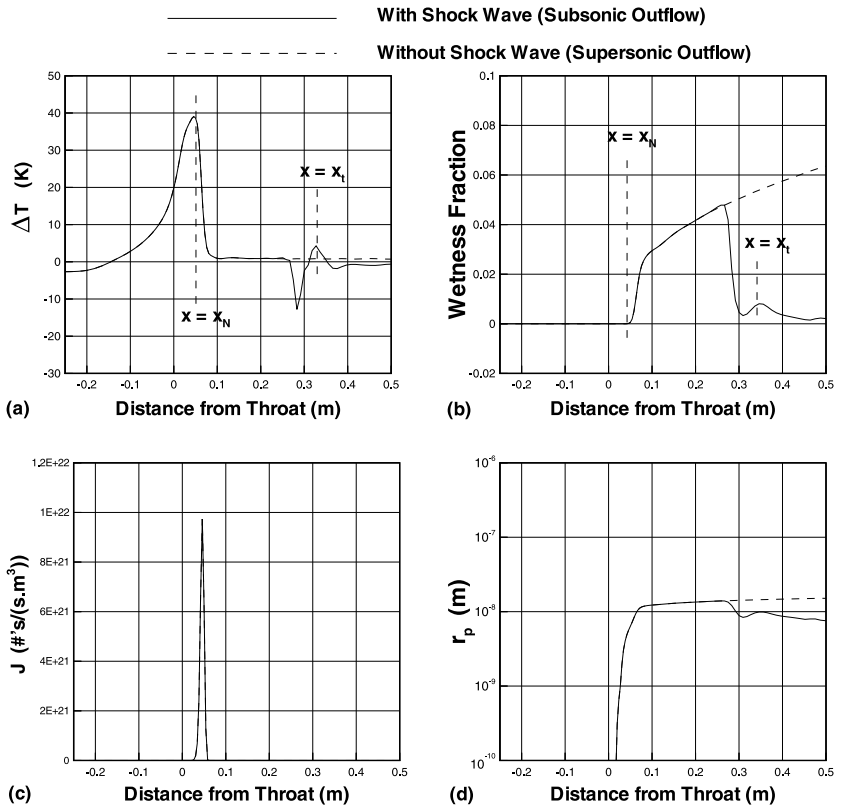

Fig. 8. Centerline values for supersonic and subsonic outflow cases of nozzle (A): (a) supercooling level, (b) wetness fraction, (c) droplet nucleation rate, and (d) droplet radius.

gas phase as condensation continues on the droplet surfaces.

In the case with a normal shock, the flow conditions upstream of the shock are, as expected, the same as those for supersonic outflow case (in Figs. 8 and 9 the lines for the supersonic- and subsonic-outflow cases coincide up to the shock location). Through the shock the supercooling level abruptly becomes negative (superheated conditions) and liquid droplets rapidly evaporate in response to the rapid pressure and temperature rise across the shock. Downstream of the shock, supercooling occurs again (with another peak point) due to reacceleration of the flow around a recirculation bubble generated as a result of shock impingement on the wall, and boundary layer separation. This is shown in Fig. 10, where the recirculation bubble takes on a shape similar to a converging–diverging nozzle to the core flow with its "throat" at location x_t. In the case of a very strong shock, the subsequent flow through this "nozzle" could reaccelerate to supersonic flow conditions and revert back to subsonic flow via a second shock, see for example Ref. [18]. In the present case, the shock is not very strong and the flow slightly accelerates up to the "throat" located at x_t followed by deceleration with the flow remaining always subsonic.

In the region between the shock and location x_t, wetness fraction and droplet size slightly increase as shown in Fig. 8(b) and (d). For $x > x_t$ the decelerating subsonic flow experiences a pressure rise, in which wetness fraction reduces and liquid droplets evaporate to smaller sizes (see Fig. 8(b) and (d)). As opposed to the supersonic outflow case, the small negative value of ΔT downstream of the shock is a physical requirement to support heat movement toward the liquid phase as evaporation continues on droplet surfaces (see Fig. 8(a)).

Fig. 9(a) shows the frozen Mach number distribution (Mach number calculated based on dry phase conditions) along the nozzle centerline, denoted by M_f. As shown in this figure, dry flow smoothly accelerates within the converging portion of the nozzle, passes the sonic condition at the throat, and continues accelerating up to $M_f \approx 1.3$, at which nucleation takes place at location x_N. Following the nucleation process, rapid release of latent heat toward the dry phase suddenly reduces the frozen Mach number while increasing pres-

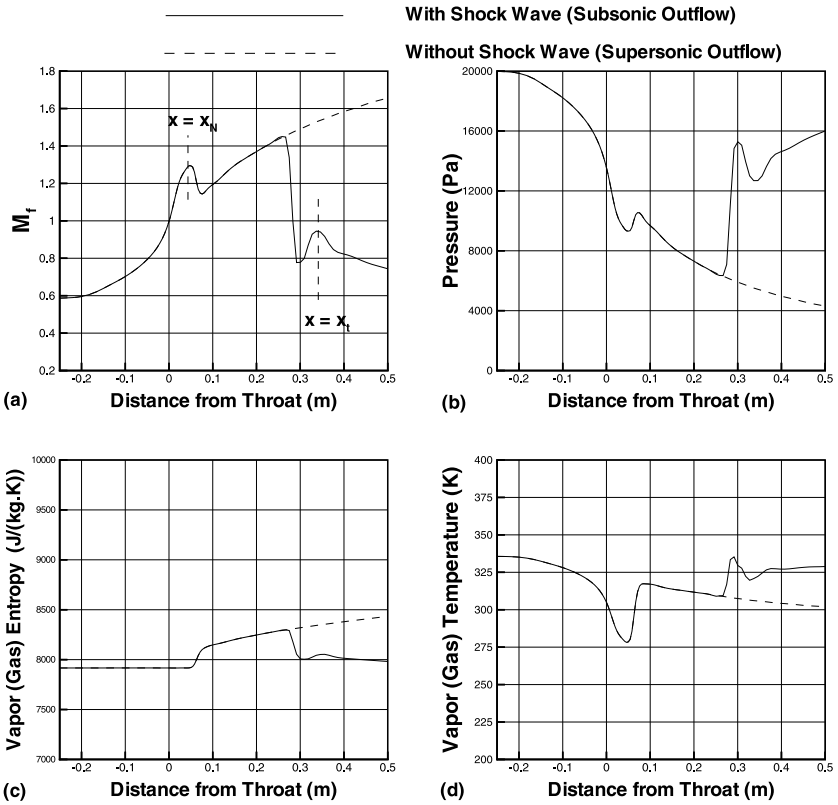

Fig. 9. Centerline values for supersonic and subsonic outflow cases of nozzle (A): (a) frozen Mach number, (b) pressure, (c) dry phase entropy, and (d) dry phase temperature.

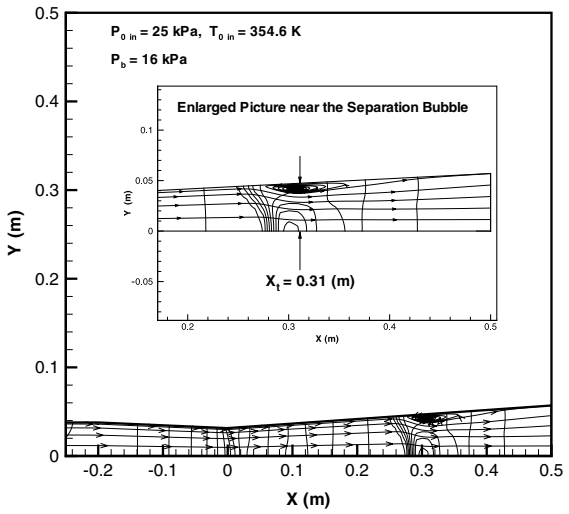

Fig. 10. Streamline and isobar lines in nozzle (A) with a normal shock. The separation bubble behind the shock makes the core flow look like a converging–diverging nozzle.

sure and the gas phase temperature as shown in Fig. 9(a), (b), and (d). This rapid response behaves similar to a normal shock wave, and is often termed a condensation shock since it occurs in response to homogeneous nucleation in a two-phase system. However, unlike a normal shock, in which the post shock condition is subsonic, in a condensation shock the post shock condition could be sonic at most.

Fig. 9(c) shows the gas phase entropy distribution along the nozzle centerline. As shown in this figure, no entropy rise is observed along the centerline up to the nucleation point. Following nucleation there is a sharp rise in the gas phase entropy due to rapid release of latent heat toward the gas phase. The gas phase entropy grows with a slower rate as the flow approaches equilibrium condition ($\Delta T = 0^+$) as shown in Fig. 8(a). For the case with normal shock, the gas phase entropy decreases within the shock in response to evaporation of the liquid phase, but the overall mixture entropy (not shown here) rises across the shock.

4.2. Thermodynamic and aerodynamic losses in steam flow with shocks

To examine the relative levels of the thermodynamic and aerodynamic losses present in nucleating flow, with

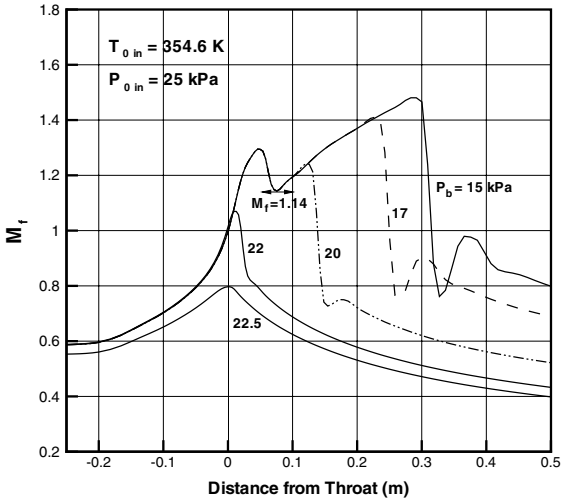

Fig. 11. Frozen Mach number (M_f) profile along the centerline of nozzle (A) for various back pressure values.

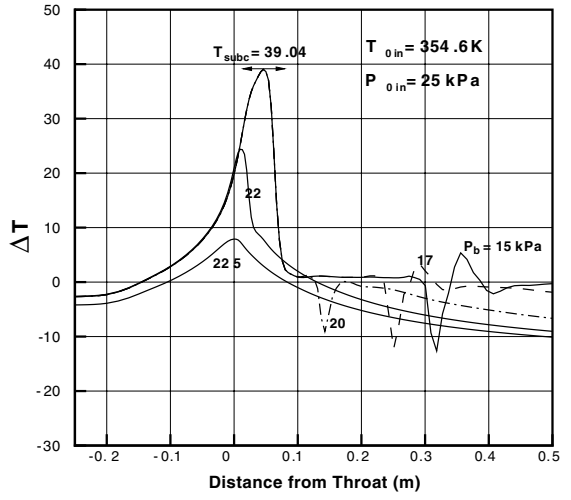

Fig. 12. Supercooling level ($\Delta T = T_{sat} - T_g$) profile along the centerline of nozzle (A) for various back pressure values.

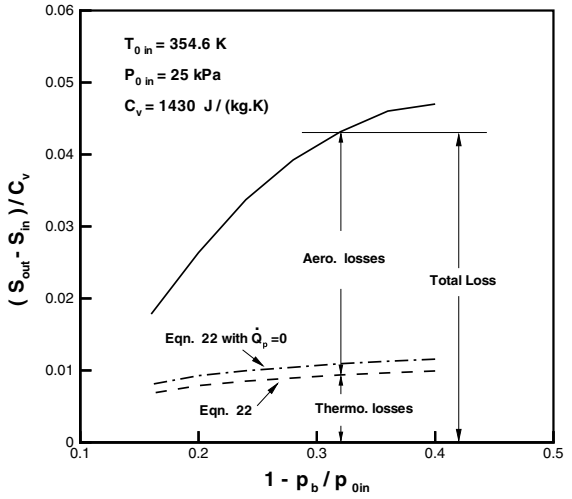

Fig. 13. Thermodynamic, aerodynamic, and total losses for different back pressure values for non-equilibrium condensing steam flow with shock in nozzle (A).

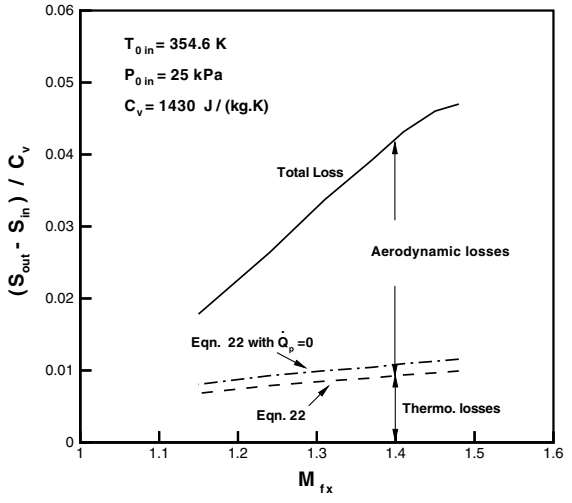

Fig. 14. Thermodynamic, aerodynamic, and total losses vs. frozen Mach number upstream of the shock (M_{f_x}) for non-equilibrium condensing steam flow with shock in nozzle (A).

and without shocks, nozzle (A) is used (see Fig. 1). With inflow conditions $P_{0_{in}} = 25$ kPa and $T_{0_{in}} = 354.6$ K results were obtained for a series of back pressures, where for each back pressure the total and thermodynamic losses were calculated.

Figs. 11 and 12 show the distribution of frozen Mach number (M_f) and the level of supercooling (ΔT) along the centerline of the nozzle for different back pressures. Normalized mass averaged values of entropy rise throughout the nozzle (normalized w.r.t. mass flow rate and $C_v = 1430$ J/kg K) are also shown in Figs. 13 and 14. In these figures the solid-line represents total losses obtained from Eq. (27), and the dashdot-line and dashed-line represent the thermodynamic losses obtained from Eq. (24) with and without $\dot{q}_p = 0$, respectively. Aerodynamic losses (losses due to viscous effects and shocks) are not directly calculated but are deduced from the difference between the total loss and the thermodynamic loss as depicted in Figs. 13 and 14. As described in Section 2.5, assuming $\dot{q}_p = 0$ ignores the fact that some portion of latent heat of the condensing layer of Region 2 (see Fig. 2) flows inside the droplet itself, and raises the temperature of the liquid droplet. This simplification deteriorates the estimation of thermodynamic loss by

10%, as shown in Figs. 13 and 14, and correspondingly the evaluation of aerodynamic loss is underestimated.

As the back pressure decreases the normal shock moves toward the nozzle exit, and the strength of the shock increases. Therefore, the fluctuations in the supercooling field (ΔT) following the shock increase (see Fig. 12), contributing to the gradual increase in thermodynamic loss, as seen in Fig. 13. It should be noted that a recirculation bubble downstream of the shock (similar to that shown in Fig. 10) increases in size with increasing strength in the shock, and contributes to the post shock oscillations in the supercooling level. The gradual increase in thermodynamic loss with reduced back pressure begins from a base level of thermodynamic loss associated with the homogeneous nucleation of moisture. This level of loss is unaffected by the position or strength of the normal shock located after the nucleation zone. The aerodynamic losses however increase rapidly with decrease in back pressure reflecting the increased strength of the shocks and higher viscous losses in the boundary layer.

5. Concluding remarks

Non-equilibrium condensing steam flow has been numerically studied in a series of converging–diverging nozzles from the perspective of quantifying loss mechanisms in such flows. A formula for the calculation of thermodynamic loss in the context of a CFD solution has been developed, which along with predicted total flow losses, allows the total aerodynamic loss to be calculated. The presented approach provides a means to assess the relative influence of aerodynamic and thermodynamic losses in condensing flows when shocks are present. Although the case of normal shocks in steam devices such as turbines is not common, the approach tested here is not limited to normal shocks and can be applied to more general situations with oblique shocks in turbines. The model highlights the fact that beyond the initial thermodynamic loss associated with homogeneous nucleation, additional, but much smaller loss, is associated with the perturbation of the two-phase temperature field through a shock.

The magnitude of the aerodynamic losses (for the converging/diverging nozzle studied) constituted 50–80% of total losses depending on the strength of the shock present in the flow conditions where the lower contribution is associated with weaker shocks. It should be mentioned that the results presented in this paper assumes small sub-micron particles resulting from homogenous nucleation. A complete analysis should also include the effects of larger droplet sizes, which introduce an additional loss due to inertial non-equilibrium between the phases. Preliminary development work has begun on this aspect of condensing flow utilizing the multiphase model of Ref. [3], which allows for slip conditions between the phases.

Acknowledgement

The financial support for this research was provided by NSERC grant # 238656-01.

References

[1] A.J. White, J.B. Young, Time-marching method for the prediction of two-dimensional, unsteady flows of condensing steam, J. Propul. Power 9 (4) (1993) 579–587.
[2] F. Bakhtar, M.R. Mahpeykar, K.K. Abbas, An investigation of nucleating flows of steam in a cascade of turbine blading-theoretical treatment, ASME J. Fluids Eng. 117 (1995) 138–144.
[3] A.G. Gerber, Two-phase Eulerian/Lagrangian model for nucleating steam flow, ASME J. Fluids Eng. 124 (2002) 465–475.
[4] F. Bakhtar, M. Ebrahimi, B.O. Bamkole, On the performance of a cascade of turbine rotor tip section blading in nucleating steam. Part 2: Wake traverses, Proc. Inst. Mech. Eng., Part C: J. Mech. Eng. Sci. 209 (1995) 169–177.
[5] A.J. White, J.B. Young, P.T. Walters, Experimental validation of condensing flow theory for a stationary cascade of steam turbine blades, Philos. Trans. R. Soc. London 354 (1996) 59–88.
[6] B.E. Launder, D.B. Spalding, The numerical computation of turbulent flows, Comp. Meth. Appl. Mech. Eng. 3 (1974) 269–289.
[7] M.P. Vukalovich, Thermodynamic Properties of Water and Steam, sixth ed., Mashgis, Moscow, 1958.
[8] F. Bakhtar, M. Piran, Thermodynamic properties of supercooled steam, Int. J. Heat Fluid Flow 1 (2) (1979) 53–62.
[9] A.G. Gerber, Modeling the steady and transient dynamics of nucleating two-phase steam flow, in: Proceedings of ASME NHTC'00 34th National Heat Transfer Conference, 20–22 August, Pittsburgh, Pennsylvania, 2000.
[10] J.E. McDonald, Homogeneous nucleation of water vapor condensation. I. Thermodynamic aspects, Am. J. Phys. 30 (1962–63) 870–877.
[11] G. Gyarmathy, Condensation in flowing steam, in: M.J. Moore, C.H. Sieverding (Eds.), A von Karman Institute Book on Two-Phase Steam Flow in Turbines and Separators, Hemisphere, 1976, pp. 127–189.
[12] J.B. Young, The spontaneous condensation of steam in supersonic nozzles, PCH (Physicochem. Hydrodyn.) 3 (1) (1982) 57–82.
[13] M.J. Moore, P.T. Walters, R.I. Crane, B.J. Davidson, Predicting the fog drop size in wet steam turbines, Institute of Mechanical Engineers (UK), Wet Steam 4 Conf., University of Warwick, 1973, paper C37/73.

[14] J.B. Young, Two-dimensional, non-equilibrium, wet-steam calculations for nozzles and turbine cascades, ASME J. Turbomachin. 114 (1992) 569–579.
[15] M.J. Raw, A coupled algebraic multigrid method for the 3D Navier-Stokes equations, in: Proceedings of the Tenth GAMM-Seminar Kiel, 14–16 January, Notes on Numerical Fluid Mechanics, vol. 49, Vieweg-Verlag, Braunschweig, Wiesbaden, Germany, 1995.
[16] G. Gyarmathy, H. Meyer, Spontane Kondensation, VDI Forschungsheft, 508, VDI-Verlag, Dusseldorf, 1965.
[17] J.D. Anderson Jr., Fundamentals of Aerodynamics, second ed., McGraw-Hill, 1991 (Chapter 9).
[18] B.F. Carroll, P.A. Lopez-Fernandez, J.C. Dutton, Computations and experiments for a multiple normal shock/boundary-layer interaction, J. Propul. Power 9 (1993) 405–411.